Generation of extreme-ultraviolet beams with time-varying orbital angular momentum

Authors: Laura Rego[1,*,†], Kevin M. Dorney[2,*,†], Nathan J. Brooks[2], Quynh L. Nguyen[2], Chen-Ting Liao[2], Julio San Román[1], David E. Couch[2], Allison Liu[2], Emilio Pisanty[3], Maciej Lewenstein[3,4], Luis Plaja[1], Henry C. Kapteyn[2], Margaret M. Murnane[2], Carlos Hernández-García[1]

Affiliations:

[1]Grupo de Investigación en Aplicaciones del Láser y Fotónica, Departamento de Física Aplicada, University of Salamanca, Salamanca E-37008, Spain

[2]JILA, Department of Physics, University of Colorado and NIST, Boulder, Colorado 80309, USA

[3]ICFO, Institut de Ciencies Fotoniques, The Barcelona Institute of Science and Technology, Av. Carl Friedrich Gauss 3, 08860 Castelldefels (Barcelona), Spain

[4]ICREA, Pg. Lluís Companys 23, 08010 Barcelona, Spain

*laura.rego@usal.es; kevin.dorney@colorado.edu

[†]These authors contributed equally to this work

One Sentence Summary: Twisted light beams carrying a controlled self-torque can be generated through high-harmonic generation.

Abstract: Light fields carrying orbital angular momentum (OAM) provide powerful capabilities for applications in optical communications, microscopy, quantum optics and microparticle manipulation. We introduce a property of light beams, manifested as a temporal OAM variation along a pulse: the self-torque of light. Although self-torque is found in diverse physical systems (i.e., electrodynamics and general relativity), it was not realized that light could possess such a property. We demonstrate that extreme-ultraviolet self-torqued beams arise in high-harmonic generation driven by time-delayed pulses with different OAM. We monitor the self-torque of extreme-ultraviolet beams through their azimuthal frequency chirp. This class of dynamic-OAM beams provides the ability for controlling magnetic, topological and quantum excitations, and for manipulating molecules and nanostructures on their natural time and length scales.

Introduction

Structured light is critical for a host of applications in imaging and spectroscopy, as well as enhancing our ability to optically manipulate macro- to nano-scale objects such as particles, molecules, atoms and electrons. The novel phase and intensity properties of structured light beams achieved by exploiting the angular momentum of light have garnered renewed interest in optical manipulation and control (*1*). One of the most relevant structured light beams are those carrying orbital angular momentum (OAM), also known as vortex beams (*2*). The OAM of light manifests from a spatially dependent wavefront rotation of the light beam, which is characterized by the phase winding number, or topological charge, ℓ. OAM beams have been harnessed for applications in diverse fields (*3*) such as laser communication (4, 5), phase-contrast (*6, 7*) and superresolution microscopy (*8*), kinematic micromanipulation (*9*), quantum information (*10*), and lithography (*10*). Spurred by these exciting technologies, a paralleled interest in the ability to control and manipulate the OAM of ultrafast light pulses has also emerged, resulting in numerous techniques that can imprint OAM directly onto an arbitrary waveform. Diffractive and refractive optics (e.g., q-plates, spiral-phase plates, and holographic techniques) (*11-13*) can impart OAM onto waves from radio, to optical, and even x-ray (*14*) frequencies, while recent advances in high-harmonic generation (HHG) have produced attosecond extreme ultraviolet (EUV) pulses with designer OAM (*15-28*).

One of the most exciting capabilities enabled by OAM beams is their ability to exert photomechanical torques (*2, 29, 30*). Whereas the linear momentum of light can be employed to control and manipulate microscopic objects via the gradient/scattering force associated with its intensity profile, optically-induced torque manifests from angular momentum transfer between an object and a light field. This enables fundamental capabilities in advanced classical and quantum optical control and manipulation techniques, such as optical tweezers, lattices, and centrifuges (*9, 31-34*), allowing for the realization of molecular and micromechanical rotors, single particle

trafficking, and fundamental studies of atomic motion in liquids and Bose-Einstein condensates (*35*, *36*).

We theoretically predict and experimentally validate the generation of light beams that carry time-dependent OAM, thus, presenting a self-torque. This inherent property of structured light, the self-torque, $\hbar\xi$, is defined as $\hbar\xi = \hbar\, d\ell(t)/dt$, where $\hbar\ell(t)$ is the time-dependent OAM content of the light pulse. After being generated, the time-dependent OAM remains as a structural property of the light beam propagating in free space, where no interaction with external agents is present. Thus, the term self-torque refers to the inherent angular acceleration of the light beam, in an analogy with other physical systems that possess a self-induced time-variation of the angular momentum—such as the radiation reaction of charged particles (*37*) or gravitational self-fields (*38*). Although OAM is well understood as a spatial property of light beams, to date, light pulses with time-dependent OAM have not been proposed or observed. We demonstrate that the self-torque arises as a necessary consequence of angular momentum conservation during the extreme nonlinear optical process of high-order harmonic generation (HHG). In HHG, the interaction of an intense field with an atom or molecule leads to the ionization of an electronic wavepacket, which acquires energy from the laser field before being driven back to its parent ion, and emitting a high-frequency photon upon recollision (*39*, *40*). The emitted harmonic radiation can extend from the EUV to the soft x-ray regime if the emissions from many atoms add together in phase (*41-44*). The resulting comb of fully coherent harmonics of the driving field in turn yields trains of phase-locked attosecond pulses (*45*, *46*).

Self-torqued light beams naturally emerge when HHG is driven by two time-delayed infrared (IR) pulses that differ by one unit of OAM (Fig. 1). The dynamical process of HHG makes it possible to imprint a continuous time-varying OAM, where all OAM components are present—thus creating self-torqued EUV beams. Intuitively, these exotic pulses can be understood as being composed of time-ordered photons carrying consecutively increasing OAM.

The self-torque of light translates to an azimuthal frequency chirp (i.e. a spectral shift along the azimuthal coordinate) on the radiation emission—and vice versa, which allows us to quantify the self-torque by an experimental measurement of the azimuthal frequency chirp. In addition, the degree of self-torque of EUV harmonic beams can be precisely controlled through the time delay and pulse duration of the driving, IR laser pulses. The generation of light beams with self-torque opens up a route for the investigation of systems with time-varying OAM that spontaneously appear in nature (*47*), as macroscopic dynamical vortices or—due to the high frequency of the beams—microscopic ultrafast systems. For example, because short-wavelength light can capture the fastest dynamics in materials (*48, 49*), self-torqued EUV beams can be expected to be used for imaging magnetic and topological excitations, for launching selective and chiral excitation of quantum matter (*50*), imprinting OAM centrifuges (*32*), switching superpositions of adiabatic charge migration in aromatic or biological molecules (*51, 52*), or for manipulating the OAM dichroism of nanostructures (*53*) on attosecond timescales.

Theory underlying the self-torque of light

In order to create light beams with self-torque, we drive the HHG process with two linearly polarized infrared (IR) pulses exhibiting the same frequency content (centered at $\omega_0 = 2\pi c/\lambda_0$), but with different OAM, ℓ_1 and ℓ_2, where $|\ell_1 - \ell_2| = 1$. The two laser pulses are separated by a variable time delay, t_d, which is on the order of the individual pulse widths (Fig. 1A) (see also section S1 in (*54*)). These two collinear IR vortex beams are then focused into an atomic gas target, such that the transverse intensity distribution of the two drivers exhibits maximum overlap. We model the HHG process using full quantum simulations in the strong-field approximation (SFA) that include propagation via the electromagnetic field propagator (*55*), a method that was used in several previous calculations of HHG involving structured pulses (*16, 18, 20, 21, 26, 28, 44, 56*). We consider the driving vortex pulses possessing $\ell_1 = 1$ and $\ell_2 = 2$, described by a $\sin^2$ envelope with τ = 10 fs full-width at half-maximum (FWHM) in intensity, centered at λ_0= 800 nm, and

delayed by $t_d = \tau$ = 10 fs (see Methods for further details). In Fig. 1A we show a schematic of the temporal envelopes of each pulse (red), as well as their superposition (blue). Figure 1C shows the time-dependent OAM of the 17th harmonic obtained from our simulations (color scale), whereas in Fig. 1B the spatial intensity distribution of the 17th harmonic is sketched at three instants of time during the emission process. In order to extract the temporal variation of the OAM, we first select the HHG spectrum in the frequency range $(q-1)\omega_0$ to $(q+1)\omega_0$ (where q is the harmonic order to explore, being q=17 in Fig. 1), and then we perform a Fourier transform along the azimuthal coordinate (*20*) at each time instant along the harmonic pulse. Remarkably, the temporal variation of the OAM is monotonic and continuous, spanning over an entire octave of consecutive topological charges—i.e., it includes all OAM components from $q\ell_1$=17 to $q\ell_2$=34.

The nature of self-torqued beams can be understood through a simple theoretical analysis. Previous works in OAM-HHG have demonstrated that an IR vortex beam can be coherently converted into high-frequency vortex beams (*15-28*). When HHG is driven by a single, linearly polarized, IR vortex beam with integer topological charge, ℓ_1, the OAM of the q^{th}-order harmonic follows a simple scaling rule, $\ell_q = q\ell_1$ (*16, 17*). This scaling reflects the nature of OAM conservation in HHG, where q IR-photons combine to produce the q^{th}-order harmonic. If HHG is driven by the combination of two collinear and temporally overlapped IR vortices with different OAM, ℓ_1 and ℓ_2, each harmonic order will span over a wide OAM spectrum, given by $\ell_q = n_1\ell_1 + n_2\ell_2$ (*20*), where n_1 and n_2 are the number of photons absorbed from each driver ($n_1 + n_2 = q$, whose totally must be odd due to parity restrictions). Each channel, (n_1, n_2), is weighted according to a binomial distribution, associated with the different combinations of absorbing n_1 photons with ℓ_1 and n_2 photons with ℓ_2. Note that the effect of the harmonic intrinsic phase in the OAM spectrum, also explored in (*20*), is second-order, negligible for the results presented here.

In this work, we consider the HHG fields that can be produced by two IR laser vortex pulses separated by some time delay. The superposition of the delayed envelopes turns into a

temporal dependence in the relative weights of the driving fields—thus introducing time as an additional parameter. To show how this influences the OAM structure of the EUV harmonics, we consider two time-delayed, collinear, linearly-polarized, IR driving pulses with different OAM, ℓ_1 and ℓ_2. We denote, in cylindrical coordinates (ρ, ϕ, z), the complex amplitudes of the driving fields at the focus position (z=0) as $U_1(\rho, \phi, t)$ and $U_2(\rho, \phi, t)$. For simplicity, we consider the field amplitudes at the ring of maximum intensity at the target—where the HHG efficiency is highest—and the resulting field can be written as $U(\phi, t) = U_0(t)\{[1-\eta(t)]e^{i\ell_1\phi} + \eta(t)e^{i\ell_2\phi}\}$, where $U_0(t) = U_1(t) + U_2(t)$ and $\eta(t) = U_2(t)/U_0(t)$ is the relative amplitude of the second beam. According to the strong-field description of HHG, the amplitude of the q^{th}-order harmonic, $A_q(\phi, t)$ scales non-perturbatively with that of the driving laser, with an exponent $p<q$ ($p\simeq4$ for our laser parameters (*20*)), while the q^{th}-order harmonic phase is considered to be q times that of the driver (see Section S1 in (*54*) for the complete derivation), thus

$$A_q(\phi, t) \propto U_0^p(t)\left[\sum_{r=0}^{p}\binom{p}{r}(1-\bar{\eta}(t))^r e^{ir\ell_1\phi}\bar{\eta}^{(p-r)}(t)e^{i(p-r)\ell_2\phi}\right]e^{i(q-p)[(1-\bar{\eta}(t))\ell_1+\bar{\eta}(t)\ell_2]\phi} \quad [1]$$

where r is an integer and $\bar{\eta}(t)$ is the average of $\eta(t)$ over the time it takes the ionized electron to complete the rescattering trajectory that contributes to the generation of a particular harmonic. For this average, we have considered the so-called short trajectories (*57, 58*), whose excursion time can be approximated to half a cycle. Note that the contribution of long trajectories to the OAM content is two orders of magnitude weaker than that of the short ones (*20*). The summation in Eq. 1 is carried over p different OAM channels, each weighted by a binomial distribution according with the combinatory nature of the HHG up-conversion process. Note that parity conservation in HHG demands that the total number of photons absorbed from each driving field, n_1+n_2, must be odd, which implies that in order to generate all intermediate OAM states between $q\ell_1$ and $q\ell_2$, the OAM of the drivers must differ by one unit, i.e. $|\ell_1 - \ell_2|$=1. The mean OAM of the q^{th}-order harmonic at any instant of time along the harmonic pulse is given by (see (*54*))

$$\bar{\ell}_q(t) = q[(1-\bar{\eta}(t))\ell_1 + \bar{\eta}(t)\ell_2] \quad [2]$$

and the width of the OAM distribution is

$$\sigma_{\ell_q} = |\ell_2 - \ell_1| \sqrt{p\bar{\eta}(t)(1-\bar{\eta}(t))} \quad [3]$$

In analogy with mechanical systems, we characterize the time-varying OAM spectrum of the q^{th}-order harmonic via the self-torque

$$\xi_q = d\bar{\ell}_q(t)/dt \quad [4]$$

Note that as the OAM of light is defined as $\hbar\ell$, the self-torque is given by $\hbar\xi$. For simplicity we factor out $\hbar$ and denote the self-torque by ξ, in units of fs^{-1}. On the other hand, it is worth mentioning that σ_{ℓ_q} depends weakly on the harmonic order, as the parameter p remains almost constant along the non-perturbative spectral plateau. The non-perturbative nature of the HHG process reduces the number of available channels to generate the q^{th}-order harmonic from q (perturbative) to p~4 (non-perturbative). As typically $p<<q$, $\bar{\ell}_q(t)$ appears as a well-defined quantity whose relative error, $\sigma_{\ell_q}/\bar{\ell}_q$, decreases as the harmonic order increases. Thus, $\bar{\ell}_q(t)$ approaches the classical behavior, i.e. its relative uncertainty tends to 0 in the limit of large harmonic orders, converging to in perfectly-defined intermediate OAM states.

In Fig. 1C, we show the temporal evolution of the mean OAM of the 17$^{\text{th}}$ harmonic, $\bar{\ell}_{17}$ (solid-green line), and its OAM width, $\sigma_{\ell_{17}}$ (dashed-green lines). In this case, where $t_d = \tau$, we can approximate the self-torque as constant over the OAM span:

$$\xi_q \sim q(\ell_2 - \ell_1)/t_d, \quad [5]$$

which provides a straightforward route for controlling the self-torque through the OAM of the driving pulses and their temporal properties. The example shown in Fig. 1C corresponds to a self-torque of $\xi_{17} = 1.32\ \text{fs}^{-1}$, which implies an attosecond variation of the OAM. Note that Eq. 5 is valid only if $t_d \simeq \tau$, and if this condition is relaxed, the self-torque must be calculated from the definition given by Eq. 4. Actually, $t_d = \tau$ is a particularly interesting case, as it corresponds to the time delay where the weight of all intermediate OAM states is more uniform over all the OAM

span (see Fig. S1 in (*54*) for the time-dependent OAM for different time delays, showing a consistently excellent agreement between the full quantum simulations and the OAM content predicted by Eq. 2 and 3).

It is important to stress that even though the mean OAM value at each instant of time may be non-integer, the nature of self-torqued beams is different from that of the well-known fractional OAM beams (*21, 59-61*). In particular, the mere superposition of two time-delayed vortex beams—carrying $\ell_i = q\ell_1$ and $\ell_f = q\ell_2$ units of OAM respectively—does not contain a self-torque. Although it does lead to a temporal variation of *the average OAM* similar as in Eq. 2, it does not contain physical intermediate OAM states, i.e. photons with OAM other than ℓ_i and ℓ_f. Self-torqued beams, on the other hand, contain all intermediate OAM states, which are time-ordered along the pulse (see Fig. 1C).

In addition, the width of the instantaneous OAM distribution of self-torqued beams (Eq. 3) is much narrower than that of the mere superposition of two time-delayed OAM beams—which in the case of $\ell_i = q\ \ell_1$ and $\ell_f = q\ \ell_2$ is $\sigma_{\ell_q} = q|\ell_2 - \ell_1|\sqrt{\eta(1-\eta)}$. This is a result of the non-perturbative behavior of HHG, that enables the creation of well-defined intermediate OAM states in a self-torqued beam. In the Movie 1 (and in Figs. S3 and S4 of (*54*)) we further evidence the distinctions in the temporal evolution of the OAM content and phase and intensity profiles between self-torqued beams and the mere superposition of two time-delayed OAM beams. In the latter case, the phase and intensity profiles remain q-fold symmetric, whereas in self-torqued beams the q-fold symmetry is broken. This breakdown in rotational symmetry is manifested in both the intensity distribution and the corresponding phase profiles of the self-torqued beams. While the intensity distribution exhibits a characteristic "crescent" shape (due to the coherent combination of vortex beams with subsequent OAM charges ($\ell_i + \ell_{i+1}$, as previously shown in Fig. 1), the associated phase profiles show the continuous appearance of new vortex singularities along a single row. In

other words, a self-torqued beam can be understood as a topological structure where new vortices emerge one at a time.

It is of paramount relevance to evidence the physical nature of the self-torqued beams by temporally characterizing the intermediate OAM states, $\ell_q(t_k)$, with $q\ell_1 < \ell_q(t_k) < q\ell_2$. Assuming a beam with constant self-toque ξ_q, the component of the q^{th}-order harmonic carrying an OAM of $\ell_q(t_k)$ will appear at the time $t_k = \frac{\ell_q(t_k) - q\ell_1}{\xi_q}$ after the peak amplitude of the first driving pulse, exhibiting a temporal width, according to Eq. 3, of $\Delta t_k = \frac{\sigma_{\ell_q}}{\xi_q} = \tau \frac{\sqrt{p\bar{\eta}(1-\bar{\eta})}}{q} \ll \tau$. Therefore, a self-torqued pulse can be thought as a pulse with a time-dependent OAM, and with a temporal OAM variation much smaller than the width of the driving pulses, reaching the attosecond timescale for sufficiently high values of self-torques. This allows us to stress the difference between self-torqued beams and a train of non-overlapping pulses with different OAM (*62*). Finally, in analogy to polarization gating techniques (*63*), self-torqued EUV beams open the possibility of sub-femtosecond OAM-gating techniques, providing an unprecedented temporal control over laser-matter interactions involving OAM.

The azimuthal frequency chirp of self-torqued beams

A direct consequence of self-torque is the presence of an azimuthal frequency chirp in the light beam. As the phase term associated with a time-dependent OAM is given by $\ell_q(t)\phi$, the instantaneous frequency of the q^{th}-order harmonic—given by the temporal variation of the harmonic phase, $\varphi_q(t,\phi)$—is shifted by the self-torque as:

$$\omega_q(t,\phi) = \frac{d\varphi_q(t,\phi)}{dt} = \omega_q + \frac{d\ell_q(t)}{dt}\phi \approx \omega_q + \xi_q\phi \qquad [6]$$

Therefore, the harmonics experience an azimuthal frequency chirp whose slope is the self-torque. Note that although $\omega_q(t,\phi)$ in Eq. 6 is a continuous function of ϕ ($-\pi \leq \phi < \pi$), the null intensity region in the crescent profile of the beam (see inset in Fig. 2A) avoids the frequency discontinuity. However, further studies on this region of "structured darkness" (*61*) could be

beneficial for a thorough fundamental understanding of self-torqued beams.

We present in Fig. 2 the HHG spectrum along the azimuthal coordinate obtained in our full quantum simulations for driving pulses of τ =10 fs and time delays of (A) $t_d = \tau = 10$ fs and (B) $t_d = -\tau = -10$ fs, respectively. The intensity crescent shape of the whole HHG beam is shown in the inset of Fig. 2A. Both spectra reflect the presence of an azimuthal chirp that depends on the harmonic order, and thus, an associated self-torque, whose sign depends on t_d. The full quantum simulations are in perfect agreement with the analytical estimation given by Eq. 6 (grey dashed lines). This result shows that the spectral bandwidth of the harmonics can be precisely controlled via the temporal and OAM properties of the driving pulses. Moreover, it provides a direct, experimentally measurable parameter to extract the self-torque, without measuring the OAM of each harmonic at each instant of time with subfemtosecond resolution, which is currently unfeasible. Of course, this reasoning implies that a beam with azimuthal frequency chirp would also exhibit self-torque. Up to now, however, HHG beams have only been driven either by spatially chirped pulses (such as the so-called "attosecond lighthouse" technique (*64, 65*)), or angularly chirped pulses through simultaneous spatial and temporal focusing, which (in theory) yield spatially chirped harmonics (*66*). However, to the best of our knowledge, azimuthal chirp—and thus, self-torque—has not been imprinted into EUV harmonics, nor in any other spectral regime.

Experimental confirmation of the self-torque of EUV beams

Light beams possessing a self-torque were experimentally generated by driving the HHG process in argon gas using two collinear, IR vortex beams with topological charges ℓ_1=1 and ℓ_2=2 that are derived from a high-power, ultrafast regenerative amplifier (Fig. 3A). Briefly (see Methods for full details), the two vortex beams are spatiotemporally overlapped to yield a mixed OAM driving mode, which is then directed onto a supersonic expansion of argon gas to generate self-torqued EUV beams (q=13-23, ~20-36 eV). The presence of self-torque in the emitted high-harmonics is confirmed by employing a cylindrical-mirror-flat-grating EUV spectrometer that serves to

transform the self-torque-induced azimuthal chirp into a spatial chirp, which is then spectrally resolved as the (1D) focusing harmonic beam is dispersed (Fig. 3B). This simultaneous mapping of the azimuthal frequency chirp and high-harmonic comb to the same spectral axis is achieved by aligning the intensity crescent of the EUV beam (see Methods and (*54*)) such that its intensity-weighted center of mass (COM) is orthogonal to the mutually parallel focusing and dispersion axes of the EUV spectrometer. In this configuration, the azimuthal frequency chirp is mapped to a linear spatial chirp by the cylindrical mirror, and this resulting spatial chirp in each harmonic is then resolved by the grating. The resulting spatial-spectral distribution is then imaged via a high-pixel-density, EUV charge-coupled device (CCD) camera, which allows for the simultaneous measurement of the azimuthal angular extent of the self-torqued beams (*54*) and the induced azimuthal frequency chirp with a high precision. High-resolution HHG spectra are collected as a function of time delay between the driving pulses by scanning the relative time delay between the two beams in two-cycle increments (i.e., 5.272 fs), which ensures the HHG beam remains aligned to the spectrometer at each experimentally sampled time delay. Such exquisite control (see Fig. S6 in (*54*)) allows us to simultaneously measure both the self-torque-induced frequency chirp of the HHG beams and the azimuthal angular range over a large range of relative time delays.

Figure 4 shows the comparison between the experimental and theoretical results. A and B show the experimental and theoretical spatial profile of the high harmonic beams, respectively. The crescent shape of the measured spatial profile already gives a clear indication of the presence of all intermediate OAM contributions from $q\ell_1$ to $q\ell_2$, and thus, of the creation of self-torqued beams. C-F show the azimuthal chirp of the high harmonics for time delays of t_d=50.4 (C, D) and -50.4 fs (E, F), respectively. The different slope of the azimuthal chirp, and the excellent agreement with the analytical theory given by Eq. 6 (grey dashed lines), and the full quantum simulations, confirm the presence of self-torque in the retrieved harmonic beams. Note that driving pulses of τ =52 fs have been used in our full quantum simulations to mimic the experimental parameters.

In Fig. 5, we plot the experimental (solid lines) and theoretical (dashed lines) self-torques obtained for the 17th (A), 19th (B), 21st (C) and 23rd (D) harmonics as a function of the time delay between the IR drivers, for the same parameters as in Fig. 4. As the time delay is varied, so too does the degree of azimuthal frequency chirp across the entire harmonic spectrum (according to Eq. 2 and 6), verifying the dynamical build-up of OAM in the self-torqued beams. Note that the self-torque is extracted from the measured azimuthal spectral shift (see Fig. 4F) and the azimuthal extent of the HHG beam (see (*54*) for details), using Eq. 6. The excellent agreement, and most importantly, the overall trend, unequivocally demonstrates the presence of a temporally evolving OAM content and, thus, a self-torque, in all the EUV harmonics generated.

Self-torque versus time duration and EUV supercontinuum generation

EUV beams with self-torque can be generated and controlled via the properties of the driving IR vortex beams, with optimal self-torque produced when the laser pulse separation is equal to their duration (i.e., $t_d = \tau$), where all intermediate OAM contributions appear with a similar weight (see Fig. S1 in (*54*)). To illustrate this concept, Fig. 6A shows the simulated self-torque obtained for different IR driving pulse durations.

In particular, if driven by few-cycle pulses, the self-torque—and thus the azimuthal chirp—is high, with large amounts of OAM building up on an attosecond timescale (Fig. 6B, where $\tau = 4$ fs). If the torque is high enough, the harmonic frequency comb sweeps along the azimuth, encapsulating all the intermediate frequencies between the teeth of the harmonic comb. Thus, the frequency chirp of time-dependent OAM beams is not only useful to measure the self-torque, but it also represents an approach to obtain an EUV supercontinuum, as shown in the right inset of Fig. 4B. This allows for the creation of a very precise, azimuthally-tunable frequency comb in the EUV, and a supercontinuum spectrum that is complementary, yet distinct, from other approaches (*67-69*).

Conclusions

We have demonstrated that light beams with time-dependent OAM can be created, thus carrying optical self-torque. This property spans the applications of structured light beams (*1*) by adding a new degree of freedom, the self-torque, and thus introducing a new route to control light-matter interactions. In particular, ultrafast, short wavelength, high harmonic beams with self-torque can be naturally produced by taking advantage of the conservation laws inherent to extreme non-linear optics. This capability can yield uniquely structured light beams that can deliver optical torque on the natural time and length scales of charge and spin ordering, e.g., femtosecond and nanometer. Finally, the self-torque of light imprints an azimuthal frequency chirp which allows a way to experimentally measure and control it. Moreover, if the self-torque is high enough, the harmonic frequency comb sweeps smoothly along the azimuth, and if integrated, a high-frequency supercontinuum is obtained, thus presenting exciting perspectives in EUV and ultrafast spectroscopies of angular momentum dynamics.

Materials and Methods

Theoretical Approach for Full Quantum Simulations Describing the Self-Torque of OAM High Harmonic Beams

In order to calculate the HHG driven by two time-delayed OAM pulses, we employ a theoretical method that computes both the full quantum single-atom HHG response and subsequent propagation (*55*). The propagation is based on the electromagnetic field propagator, in which we discretize the target (gas jet) into elementary radiators (*55*). The dipole acceleration of each elementary source is computed using the full quantum SFA, instead of solving directly the time dependent Schrödinger equation, yielding a performance gain in computational time when computing HHG over the entire target (*55*). Note that at the microscopic single-atom level, and for the parameters considered in this work, the spatial phase of the electric field can be well

approximated as homogeneous in the vicinity of the atom where the wavepacket dynamics takes place. We assume that the harmonic radiation propagates with the vacuum phase velocity, which is a reasonable assumption for high-order harmonics. Propagation effects in the fundamental field, such as the production of free charges, the refractive index of the neutrals, the group velocity walk-off, as well as absorption in the propagation of the harmonics, are taken into account. Note that although we account for the time-dependent nonlinear phase shifts in the driving fields, nonlinear spatial effects are not taken into account. We consider two vortex beams with $\ell_1 = 1$ and $\ell_2 = 2$, whose spatial structure is represented by a Laguerre-Gaussian beam (see Eq. S13 in (*54*)). The laser pulses are modeled with a $\sin^2$ envelope whose FWHM in intensity is τ, and centered at 800 nm in wavelength. The amplitudes of the two fields are chosen to obtain the same peak intensity ($1\ x\ 10^{14}$ W/cm^2) at focus for each driver at the radii of maximum superposition (i.e., the brightest intensity rings overlap spatially). The driving beam waists are chosen to overlap at the focal plane (being $w_1 = 30.0$ μm for ℓ_1, and $w_2 = w_1/\sqrt{2} = 21.4$ μm for ℓ_2) where a 10-μm-wide Ar gas jet flows along the perpendicular direction to the beam propagation, with a peak pressure of 667 Pa (5 torr). The low thickness of the gas jet is due to computational time limitations; however, based on our previous results of OAM-HHG (*18*), we do not foresee any fundamental deviation when considering thicker gas jets closer to the experimental jet employed in this work (a diameter of 150 μm).

Experimental Setup for the Generation and Characterization of Self-Torqued EUV Beams

The generation of self-torqued high-harmonics is achieved by impinging a pair of collinear, linearly polarized, non-degenerate IR-vortex beams onto a supersonic expansion of argon gas. The IR vortex beams (with topological charges of $\ell_1 = 1, \ell_2 = 2$) are derived from a high-power, ultrafast regenerative amplifier (790 nm, 40 fs, 9 mJ, 1 kHz, KMLabs Wyvern HE®). The near

full output of the amplifier is sent into a frequency-degenerate Mach-Zehnder-type interferometer, which separates and later recombines the two driving pulses to form the dual-vortex IR driver. In each spatially separated arm of the interferometer, a combination of half-waveplates, faceted spiral phase plates (16 steps per phase ramp, HoloOr), and independent focusing lenses result in each beam possessing linear polarization, non-degenerate topological charges, and similarly sized intensity rings at focus. Independent irises in each beam path allow for fine tuning of the transverse mode size at focus and are utilized to match the size of the maximum intensity ring for each driver. Using this strategy, the two driving beams possessed a full diameter of the intensity of ~65 μm—corresponding to waists sizes of w_{ℓ_1}≈45 μm and w_{ℓ_2}≈33 μm (*70*). The driving laser modes themselves, both individually and combined, are characterized by a modified Gerchberg-Saxton phase retrieval algorithm, which solves for the phase of a propagating light beam and allows extraction of the OAM content of the IR vortices (see Section S4 in (*54*)), thus ensuring high-quality vortex beams for driving the HHG process (Supplemental Movie S1). Note that this modified Gerchberg-Saxton method acquires and retrieves OAM content much faster than our previous characterization method using ptychography (*71*), but it is limited to non-multiplexed (i.e., single-color) beams. A high-precision, high-accuracy, and high-repeatability delay stage (Newport, XMS-160S) is used to control the relative time delay between the two driving pulses, with subfemtosecond precision. The pulses are recombined at the output of the interferometer using a low-dispersion beamsplitter, and then directed onto the supersonic expansion of argon gas in a vacuum chamber. We take extreme care to ensure that the two arms experience similar dispersion by utilizing the same thickness and design of optics in each arm of the interferometer, which helps to reduce effects from carrier-to-envelope phase variation in the separate beam paths, while also ensuring similar pulse widths. Finally, we note that the use of a frequency-degenerate Mach-Zehnder interferometer results in a 50% intensity loss of each driver when combined at the interferometer's exit; however, this configuration proved ideal to minimize pulse dispersion, while

also allowing for independent control of the polarization and topological charge of the driving beams.

Self-torqued high harmonics are generated via the HHG up-conversion process, then dispersed in 1D via a cylindrical-mirror-flat-grating EUV spectrometer and finally collected by a CCD camera (Andor Newton 940). A 200-nm-thick aluminum filter blocks the residual driving light before entering the spectrometer—while passing harmonics over its transmission range, ~17-72 eV—and all harmonic spectra are corrected for the transmission of the EUV beamline. In order to align the resulting HHG crescent to the spectrometer, we exploit the natural physics of time-delayed OAM beams. When two vortex beams with ℓ_1=1 and ℓ_2=2 are superposed, such that their amplitudes and intensity rings are equal, the resulting intensity distribution exhibits a characteristic crescent shape. The azimuthal orientation of the COM of the intensity crescent can be controlled via a relative phase delay between the two single-mode OAM drivers, such that a full-cycle phase delay (i.e., 2.635 fs for the 790-nm pulses used here) returns the intensity crescent to its initial position. By carefully adjusting the time delay between the two single-mode IR vortex beams, we can control the alignment of the intensity crescent of the driving beam (see (*54*)), and so to the resulting crescent-shaped harmonic beam (since, to first order, the HHG beam profile mimics the intensity distribution of the driving beam). Once the harmonic beam is aligned to the spectrometer, the relative phase delay between the driving beams is scanned in two-cycle increments (i.e., 5.272 fs), which ensures the HHG beam remains aligned to the spectrometer at each experimentally sampled time delay. Such exquisite control (see Fig. S6 in (*54*)) allows us to simultaneously measure both the self-torque-induced frequency chirp of the HHG beam and the azimuthal angular range (see (*54*), Section S7) with a high resolution.

References and Notes

1. H. Rubinsztein-Dunlop, et al., Roadmap on structured light. *J. Opt.* **19**, 013001 (2017).

2. L. Allen, M. W. Beijersbergen, R. J. C. Spreeuw, J. P. Woerdman, Orbital angular momentum of light and the transformation of Laguerre-Gaussian laser modes. *Phys. Rev. A* **45,** 8185-8189 (1992).

3. A. M. Yao, M. J. Padgett, Orbital angular momentum: origins, behavior and applications. *Adv. Opt. Photonics* **3,** 161-204 (2011).

4. A. E. Willner, et al., Optical communication using orbital angular momentum beams. *Adv. Opt. Photonics.* **7,** 66-106 (2015).

5. A. Trichili, et al., Optical communication beyond orbital angular momentum. *Sci. Rep*. **6,** 27674 (2016).

6. S. Fürhapter, A. Jesacher, S. Bernet, M. Ritsch-Marte, Spiral phase contrast imaging in microscopy. *Opt. Express.* **13** (3), 689-694 (2005).

7. M. A. Lauterbach, M. Guillon, A. Soltani, V. Emiliani, STED microscopy with spiral phase contrast. *Sci. Reports.* **3**, 2050 (2013).

8. G. Vicidomini, P. Bianchini, A. Diaspro, STED super-resolved microscopy. *Nat. Methods.* **15**, 173-182 (2018).

9. M. Padgett, R. Bowman, Tweezers with a twist. *Nat. Photonics* **5,** 343-348 (2011).

10. J. P. Torres, L. Torner, *Twisted Photons: Applications of Light with Orbital Angular Momentum.* (Bristol: Wiley-VCH, 2011).

11. L. Marrucci, C. Manzo, D. Paparo, Optical Spin-to-Orbital Angular Momentum Conversion in Inhomogeneous Anisotropic Media. *Phys. Rev. Lett.* **96**, 163905 (2006).

12. M. W. Beijersbergen, R. P. C. Coerwinkel, M. Kristensen, J.P. Woerdman, Helical-wavefront laser beams produced with a spiral phase plate. *Opt. Commun.* **112**, 321-327 (1994).

13. J. Atencia, et al., Holographic optical element to generate achromatic vortices. *Opt. Express* **21**, 21056 (2013).

14. J. C. T. Lee, S. J. Alexander, S. D. Devan, S. Roy, B. J. McMorran, Laguerre-Gauss and Hermite-Gauss soft x-ray states generated using diffractive optics. *Nat. Photon.*

https://doi.org/10.1038/s41566-018-0328-8 (2019).

15. M. Zürch, et al., Strong-field physics with singular light beams. *Nat. Phys.* 8, 743 (2012).

16. C. Hernández-García, et al., Attosecond extreme ultraviolet vortices from high-order harmonic generation. *Phys. Rev. Lett.* **111**, 083602 (2013).

17. G. Gariepy, et al., Creating high-harmonic beams with controlled orbital angular momentum. *Phys. Rev. Lett.* **113**, 153901 (2014).

18. C. Hernández-García, J. San Román, L. Plaja, A. Picón, Quantum-path signatures in attosecond helical beams driven by optical vortices. *New J. Phys.* **17,** 093029 (2015).

19. R. Géneaux, et al. Synthesis and characterization of attosecond light vortices in the extreme ultraviolet. *Nat. Commun.* **7**, 12583 (2016).

20. L. Rego, J. San Román, A. Picón, L. Plaja, C. Hernández-García, Nonperturbative twist in the generation of extreme-ultraviolet vortex beams. *Phys. Rev. Lett.* **117,** 163202 (2016).

21. A. Turpin, L. Rego, L. Picon, J. San Roman, C. Hernandez-Garcia, Extreme ultraviolet fractional orbital angular momentum beams from high harmonic generation. *Sci. Rep.* **7,** 43888 (2017).

22. F. Kong, et al., Controlling the orbital angular momentum of high harmonic vortices. *Nat. Commun.* **8,** 14970 (2017).

23. D. Gauthier, et al., Tunable orbital angular momentum in high-harmonic generation. *Nat. Commun.* **8,** 14971 (2017).

24. C. Hernández-García, A twist in coherent X-rays. *Nat. Phys.* **13**, 327 (2017).

25. R. Géneaux et al. Radial index of Laguerre-Gaussian modes in high-order-harmonic generation. *Phys. Rev. A* **95**, 051801(R) (2017).

26. K. M. Dorney, et al., Controlling the polarization and vortex charge of attosecond high-harmonic beams via simultaneous spin-orbit momentum conservation. *Nat. Photon.* **13**, 123-130 (2019).

27. W. Paufler, B. Böning, and S. Fritzsche, Tailored orbital angular momentum in high-order harmonic generation with bicircular Laguerre-Gaussian beams. *Phys. Rev. A* **98**, 011401(R) (2018).

28. E. Pisanty, et al., Conservation of torus-knot angular momentum in high-order harmonic generation, *Physical Review Letters*, in press. *arXiv:1810.06503*

29. M. Babiker, W. L. Power, L. Allen, Light-induced torque on moving atoms. *Phys. Rev. Lett*. **73**, 1239 (1994).

30. H. He, N. E. J. Friese, N. R. Heckenberg, H. Rubinsztein-Dunlop, Direct observation of transfer of angular momentum to absorptive particles from a laser beam with a phase singularity. *Phys. Rev. Lett.* **75**, 826 (1995).

31. A. T. O'Neil, M. J. Padgett, Three-dimensional optical confinement of micron-sized metal particles and the decoupling of the spin and orbital angular momentum within an optical spanner. *Opt. Commun.* **185**, 139–143 (2000).

32. D. M. Villeneuve, S. A. Aseyev, P. Dietrich, M. Spanner, M. Yu. Ivanov, P. B. Corkum, Forced molecular rotation in an optical centrifuge, *Phys. Rev. Lett.* **85**, 542-545 (2000).

33. D. G. Grier, A revolution in optical manipulation. *Nature* **424**, 21 (2006).

34. M. E. J. Friese, H. Rubinsztein-Dunlop, J. Gold, P. Hagberg, D. Hanstorp, Optically driven micromachine elements. *Appl. Phys. Lett.* **78**, 547–549 (2001).

35. E. M. Wright, J. Arlt, K. Dholakia, Toroidal optical dipole traps for atomic Bose-Einstein condensates using Laguerre-Gaussian beams, *Phys. Rev. A* **63**, 013608 (2000).

36. A. Turpin, J. Polo, Y. V. Loiko, J. Küber, F. Schmaltz, T. K. Kalandjiev, V. Ahufinger, G. Birlkl, J. Mompart, Blue-detuned optical ring trap for Bose-Einstein condensates based on conical refraction, *Opt. Express* **23**, 1638 (2015).

37. A. F. Rañada, L. Vázquez, On the self-torque on an extended classical charged particle. *J. Phys. A: Math. Gen.* **17**, 2011-2016 (1984).

38. S. R. Dolan, N. Warburton, A.I. Harte, A. Le Tiec, B. Wardell, L. Barack, Gravitational self-torque and spin precession in compact binaries, *Phys. Rev. D* **89**, 064011 (2014).

39. K. J. Schafer, B. Yang, L. F. DiMauro, K. C. Kulander, Above threshold ionization beyond the high harmonic cutoff. *Phys. Rev. Lett.* **70,** 1599–1602 (1993).

40. P. B. Corkum, Plasma perspective on strong-field multiphoton ionization. *Phys. Rev. Lett.* **71,** 1994–1997 (1993).

41. A. Rundquist, et al., Phase matching of soft X-ray harmonic emission in hollow-core fibers. *Science* **280**, 1412–1415 (1998).

42. R. A. Bartels, et al., Generation of spatially coherent light at extreme ultraviolet wavelengths. *Science* **297** (5580), 376-378 (2002).

43. T. Popmintchev, et al., Bright coherent ultrahigh harmonics in the keV x-ray regime from mid-infrared femtosecond lasers. *Science* **336,** 1287 (2012).

44. T. Fan, et al., Bright circularly polarized soft X-ray high harmonics for X-ray magnetic circular dichroism. *Proc. Natl Acad. Sci. USA* **111**, 14206–14211 (2015).

45. P. M. Paul, E. S. Toma, P. Berger, G. Mullot, F. Augé, Ph. Balcou, H. G., Muller, P. Agostini, Observation of a train of attosecond pulses from high harmonic generation. *Science* **292** (5522), 1689-1692 (2001).

46. M. Hentschel, et al., Attosecond metrology, *Nature* **414**, 509 (2001).

47. B. Rodenburg, M. P. J. Lavery, M. Malik, M. N. O'Sullivan, M. Mirhosseini, D. J. Robertson, M. Padgett, R. W. Boyd, Influence of atmospheric turbulence on states of light carrying orbital angular momentum, *Opt. Lett.* **37**, 3735-3737 (2012).

48. C. Chen, et al., Distinguishing attosecond electron–electron scattering and screening in transition metals. *Proc. Natl Acad. Sci. USA* **114**, E5300–E5307 (2017).

49. P. Tengdin, et al., Critical behavior within 20 fs drives the out-of-equilibrium laser-induced magnetic phase transition in nickel. *Sci. Adv.* **4**, 9744 (2018).

50. A. Picón, A. Benseny, J. Mompart, J. R. Vázquez de Aldana, L. Plaja, G. F. Calvo, L. Roso, Transferring orbital and spin angular momenta of light to atoms. *New. J. Phys.* **12**, 083053 (2010).

51. F. Calegari, A. Trabattoni, A. Palacios, D. Ayuso, M. C. Castrovilli, J. B. Greenwood, P. Decleva, F. Martín, M. Nisoli, Charge migration induced by attosecond pulses in bio-relevant molecules. *J. Phys. B. At. Mol. Opt.* **49**, 142001 (2016).

52. G. Hermann, C.-M. Liu, J. Manz, B. Paulus, V. Pohl, J. C. Trembley, Attosecond angular flux of partial charges on the carbon atoms of benzene in non-aromatic excited state. *Chem. Phys. Lett.* **663**, 553-558 (2017).

53. R. M. Kerber, J. M. Fitzgerald, S. S. Oh, D. E. Reiter, O. Hess, Orbital angular momentum dichroism in nanoantennas. *Comm. Phys.* **1**, 87 (2018).

54. Supplemental Material.

55. C. Hernández-García, J. A. Pérez-Hernández, J. Ramos, E. Conejero Jarque, L. Roso, L. Plaja, High-order harmonic propagation in gases within the discrete dipole approximation, *Phys. Rev. A* **82**, 0033432 (2010).

56. C. Hernández-García, et al., Extreme ultraviolet vector beams driven by infrared lasers. *Optica.* **4**, 520 (2017).

57. M. Lewenstein, P. Balcou, M. Y. Ivanov, A. L'Huillier, and P. B. Corkum, Theory of high-harmonic generation by low-frequency laser fields, Phys. Rev. A **49**, 2117 (1994).

58. A. Zaïr, M. Holler, A. Guandalini, F. Schapper, J. Biegert, L. Gallmann, U. Keller, A. S. Wyatt, A. Monmayrant, I. A. Walmsley, E. Cormier, T. Auguste, J. P. Caumes, and P. Salières, Quantum path interferences in high-order harmonic generation, Phys. Rev. Lett. **100**, 143902 (2008).

59. M. V. Berry, Optical vortices evolving from helicoidal integer and fractional phase steps. *J. Opt. A: Pure Appl. Opt.* **6**, 259 (2004).

60. J. Leach, E. Yao, M. Padgett, Observation of the vortex structure of non-integer vortex beam. *New J. Phys.* **6**, 71 (2004).

61. S. N. Alperin, M. E. Siemens, Angular Momentum of Topologically Structured Darkness. *Phys. Rev. Lett.* **119**, 203902 (2017).

62. E. Karimi, L. Marrucci, C. de Lisio, E. Santamato, Time-division multiplexing of the orbital angular momentum of light, *Opt. Lett.* **37**, 127 (2012).

63. I. J. Sola, E. Mével, L. Elouga, E. Constant, V. Strelkov, L. Poletto, P. Villoresi, E. Benedetti, J.-P. Caumes, S. Stagira, C. Vozzi, G. Sansone, M. Nisoli, Controlling attosecond electron dynamics by phase-stabilized polarization gating. *Nature Phys.* **2**, 319–322 (2006).

64. H. Vincenti, F. Quéré, Attosecond lighthouses: how to use spatiotemporally coupled light fields to generate isolated attosecond pulses. *Phys. Rev. Lett.* **108**, 113904 (2012).

65. J. A. Wheeler, et al., Attosecond lighthouses from plasma mirrors, *Nat. Photon.* **6**, 829-833 (2012).

66. C. Hernández-García, A. Jaron-Becker, D. D. Hickstein, A. Becker, C. G. Durfee, High-order-harmonic generation driven by pulses with angular spatial chirp. *Phys. Rev. A* **93**, 023825 (2016).

67. I. P. Christov, M. M. Murnane, H. C. Kapteyn, High-harmonic generation of attosecond pulses in the "single cycle" regime. *Phys. Rev. Lett.* **78**, 1251-1254 (1997).

68. M. Chini, K. Zhao, Z. Cheng, The generation, characterization and applications of broadband isolated attosecond pulses, *Nat. Photon.* **8**, 178 (2014).

69. W. Holgado, et al., Continuous spectra in high-harmonic generation driven by multicycle laser pulses, *Phys. Rev. A.* **93**, 013816 (2016).

70. J. Zhang, S.-J. Huang, F.-Q. Zhu, W. Shao, M.-S. Chen, Dimensional properties of Laguerre–Gaussian vortex beams, Appl. Opt. **56**, 3556-3561 (2017).

71. Y. Esashi, C.-T. Liao, B. Wang, N. Brooks, K. M. Dorney, C. Hernández-García, H. Kapteyn, D. Adams, M. Murnane, Ptychographic amplitude and phase reconstruction of bichromatic vortex beams. *Opt. Express.* **26** 34007 (2018).

References below this line are found in the supplementary material

72. A. L'Huillier, Ph. Balcou, S. Candel, K. J. Schafer, K. C. Kulander, Calculations of high-order harmonic-generation processes in xenon at 1064 nm. *Phys. Rev. A* **46**, 2778 (1992).

73. G. Gbur, Fractional vortex Hilbert's hotel. *Optica*. **3**, 222-225 (2016).

74. S. Fu, S. Zhang, T. Wang, C. Gao, Pre-turbulence compensation of orbital angular momentum beams based on a probe and the Gerchberg-Saxton algorithm. *Opt. Lett.* **41** (14), 3185-3188 (2016).

75. H. Chang, X.-L. Yin, X.-Z. Cui, Z.-C. Zhang, J.-X. Ma, G.-H. Wu, L.-J Zhang, X.-J. Xin, Adaptive optics compensation of orbital angular momentum beams with a modified Gerchberg-Saxton-based phase retrieval algorithm. *Opt. Commun.* **405**, 271-275 (2017).

76. M. Seaberg, M. Donald. "Nanoscale EUV Microscopy on a Tabletop: A General Transmission and Reflection Mode Microscope Based on Coherent Diffractive Imaging with High Harmonic Illumination" (2014). *Phsyics Graduate Theses & Dissertations.* 6 https://scholar.colorado.edu/phys_gradetds/6

77. E. Karimi, G. Zito, B. Piccirillo, L. Marrucci, E. Santamato, Hypergeometric-Gaussian modes. *Opt. Lett.* **32** (21), 3053-3055 (2007).

78. E. Yao, S. Franke-Arnold, J. Courtial, S. Barnett, M. J. Padgett, Fourier relationship between angular position and optical orbital angular momentum. *Opt. Express.* **14** (20), 9071-9076 (2006).

79. S. N. Alperin, R. D. Niederriter, J. T. Gopinath, M. E. Siemens, Quantitative measurement of the orbital angular momentum of light with a single, stationary lens. *Opt. Lett*. **41** (21), 5019-5022 (2016).

Acknowledgments:

Funding: C.H.-G., J.S.R. and L.P. acknowledge support from Junta de Castilla y León (SA046U16) and Ministerio de Economía y Competitividad (FIS2016-75652-P) and Ministerio de Ciencia, Innovación y Universidades (EQC2018-0041 17-P). L.R. acknowledges support from Ministerio de Educación, Cultura y Deporte (FPU16/02591). C.H.-G. acknowledges support from a 2017 Leonardo Grant for Researchers and Cultural Creators, BBVA Foundation and Ministerio de Ciencia, Innovación y Universidades for a Ramón y Cajal contract (RYC-2017-22745), co-funded by the European Social Fund. M.M. and H.K. acknowledge support from the DOE AMOS Program (DE-FG02-99ER14982) for the new light science experimental demonstration, the DARPA TEE Program (D18AC00017) for the new experimental characterization methods

developed, and an AFOSR MURI (FA9550-16-1-0121) for theory. N. J. B., Q. L. N., and D. C. acknowledge support from National Science Foundation Graduate Research Fellowships (Grant No. DGE-1144083). E.P. acknowledges Cellex-ICFO-MPQ fellowship funding; E.P. and M.L. acknowledge the Spanish Ministry MINECO (National Plan 15 Grant: FISICATEAMO No. FIS2016-79508-P, SEVERO OCHOA No. SEV-2015-0522, FPI), European Social Fund, Fundació Cellex, Generalitat de Catalunya (AGAUR Grant No. 2017 SGR 1341 and CERCA/Program), ERC AdG OSYRIS, EU FETPRO QUIC, and the National Science Centre, Poland-Symfonia Grant No. 2016/20/W/ST4/00314. We thankfully acknowledge the computer resources at MareNostrum and the technical support provided by Barcelona Supercomputing Center (RES-AECT-2014-2-0085). This research made use of the high-performance computing resources of the Castilla y León Supercomputing Center (SCAYLE, https://www.scayle.es/), financed by the European Regional Development Fund (ERDF). **Author contributions:** L.R., J.S.R, L.P. and C.H.-G. conceived the idea of self-torqued beams. K.M.D., L.R., H.C.K., M.M.M. and C.H.-G. designed the experiment. K.M.D., N.J.B., Q.N., C.-T.L., D.C., A.L. conducted the experiment. K.M.D. and N. J. B. analyzed the experimental data. L.R., J.S.R., L.P., E.P. and C.H.-G. performed the theoretical simulations and analyzed the resulting data. C.H.-G., L.P., M.L., M.M.M., and H.C.K. supervised the theoretical simulations, experimental work and developed the facilities and measurement capabilities. L.R., K.M.D., J.S.R., M.M.M., L.P. and C.H.-G. wrote and prepared the manuscript. All authors provided constructive improvements and feedback to this work. **Financial interests:** M. M. M. and H. C. K. have a financial interest in KMLabs. The other authors declare no competing financial interests. **Data and materials availability:** The datasets and analysis routines utilized to prepare the data presented in this manuscript are available, free of charge, from the corresponding authors under reasonable request.

Supplementary Materials:

Supplementary Text:

Section S1: Derivation the theoretical equation for the self-torque of light.

Section S2: Distinction between self-torqued beams and time-delayed vortex beams.

Section S3: Additional Experimental Details for the Generation and Characterization of Self-Torqued EUV Beams

Section S4: Characterization of IR Vortex Driving Modes via a Modified Gerchberg-Saxton Phase-Retrieval Algorithm

Section S5: Control of IR and HHG Beam Pointing with a Time-Delayed Combination of Vortex Driving Beams

Figures captions:

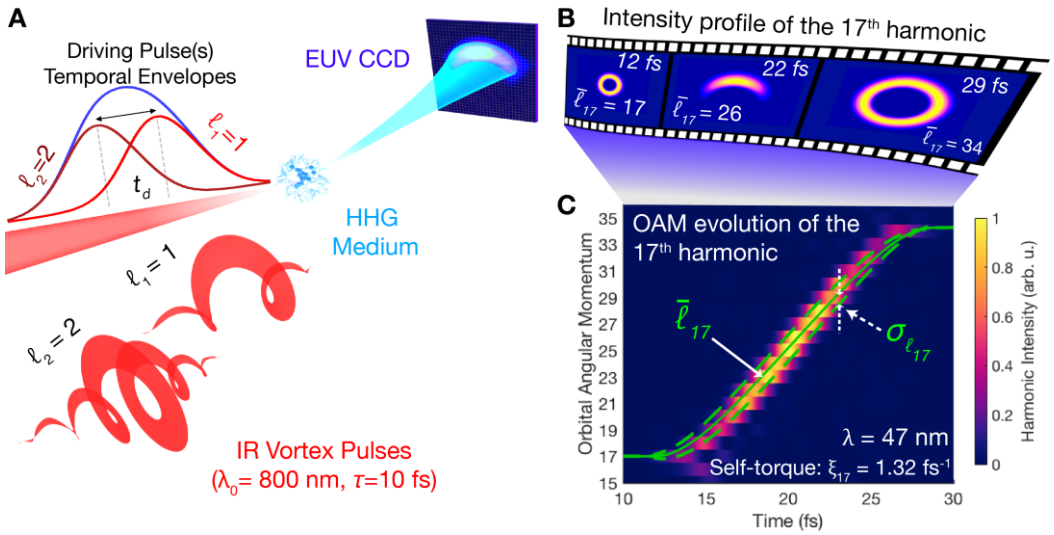

Fig.1. Generation of EUV Beams with Self-Torque. (**A**) Two time-delayed, collinear IR pulses with the same wavelength (800 nm), but different OAM values, are focused into an argon gas target (HHG medium) to produce

harmonic beams with self-torque. The spatial profile of the complete, time-integrated, HHG beam from full quantum simulations is shown on the EUV CCD. (**B**) Predicted evolution of the intensity profile of the 17th harmonic at three instants in time during the emission process. (**C**) Temporal evolution of the OAM of the 17th harmonic, for two driving pulses with the same duration $\tau = 10$ fs, at a relative time delay of $t_d = \tau$. The average OAM, $\bar{\ell}_{17}$ (solid green), and the width of the OAM distribution, $\sigma_{\ell_{17}}$ (distance between the solid and dashed-green lines), are obtained from Eq. 1 and 3. The self-torque associated with this pulse, ξ=1.32 fs^{-1}, is obtained from the slope of the smooth and continuous time-dependent OAM.

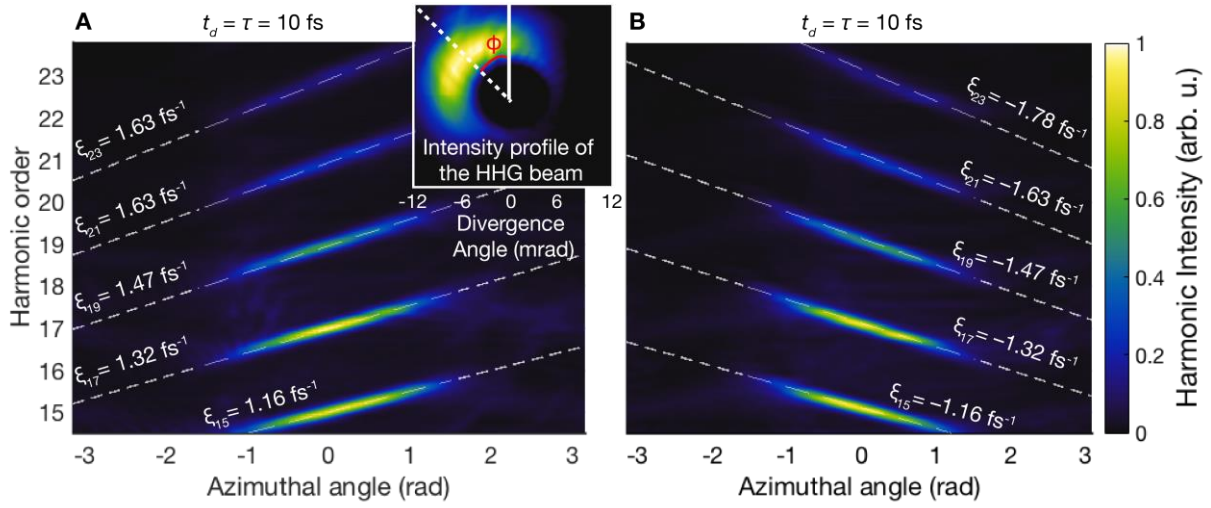

Fig. 2. Azimuthal Frequency Chirp of Self-Torqued Beams. Simulated spatial HHG spectrum along the azimuthal coordinate (ϕ) when the time delay between the driving pulses is (**A**) 10 fs and (**B**) -10 fs. The self-torque of light imprints an azimuthal frequency chirp, which is different for each harmonic, as indicated by the grey dashed lines (obtained from Eq. 6). The azimuthal frequency chirp serves as a direct measurement of the self-torque of each harmonic beam. The inset of (**A**) shows the intensity profile of the HHG beam, as well as the definition of the azimuth, ϕ.

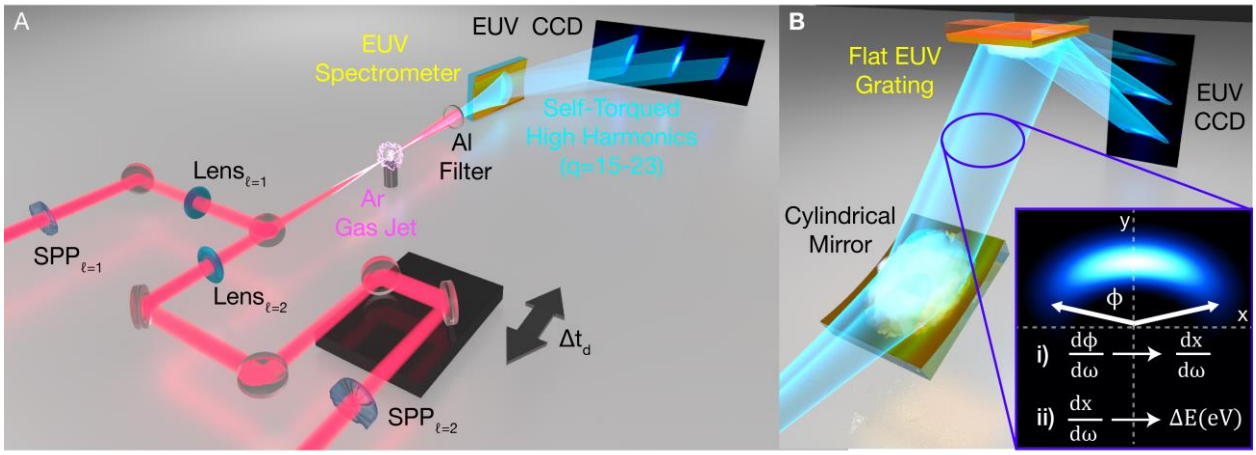

Fig. 3. Experimental Scheme for Generating and Measuring Light Beams with a Self-Torque. (**A**) Two time-delayed, collinear IR pulses with the same wavelength (790 nm), but different OAM values, are focused into an argon gas target to produce harmonic beams with self-torque. **(B)** An EUV spectrometer, composed of a cylindrical-mirror

and flat-grating pair, collapse the HHG beam in the vertical dimension (lab frame y-axis), while preserving spatial information, and thus the azimuthal extent in the transverse dimension (lab frame x-axis). (lower-right inset,) The cylindrical mirror effectively maps the azimuthal frequency chirp into a spatial chirp along the lab frame x-axis (**i**), which is then dispersed by the grating (**ii**).

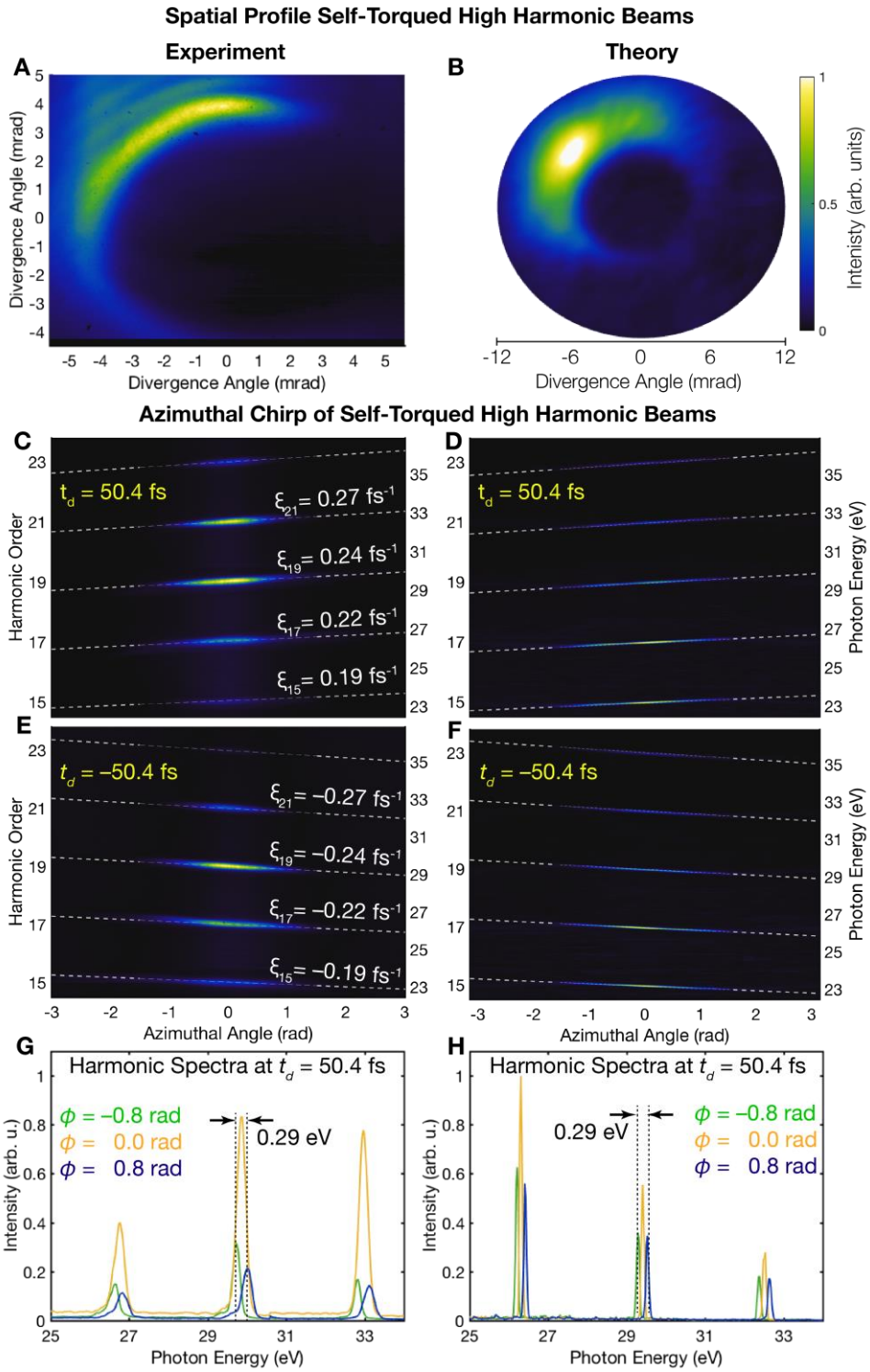

Fig. 4. Azimuthal Frequency Chirp and Experimental Measurement of the Self-Torque of EUV Beams. (**A**, **B**) Experimental and theoretical spatial intensities of the HHG beams, after passing through an Al filter, comprising

harmonics q=13-23. (**C**-**F**) Spatial HHG spectrum along the azimuthal coordinate (ϕ) from experiment (**C**, **E**) and quantum simulations (**D**, **F**), when the time delay between the driving pulses is (**C**, **D**) 50.4 fs and (**E**, **F**) -50.4 fs. The self-torque of light imprints an azimuthal frequency chirp, which is different for each harmonic, as indicated by the grey dashed lines (obtained from Eq. 6). Panels (**G**, **H**) show the theoretical and experimental harmonic lineouts obtained at ϕ=-0.8 rad (green), ϕ=0.0 rad (yellow) and ϕ=0.8 rad (blue) for t_d=50.4 fs. The azimuthal frequency chirp serves as a direct measurement of the self-torque of each harmonic beam. Differences in mode size of the theoretical and experimental EUV beam are due to slight differences in the fundamental beam mode sizes (see Methods).

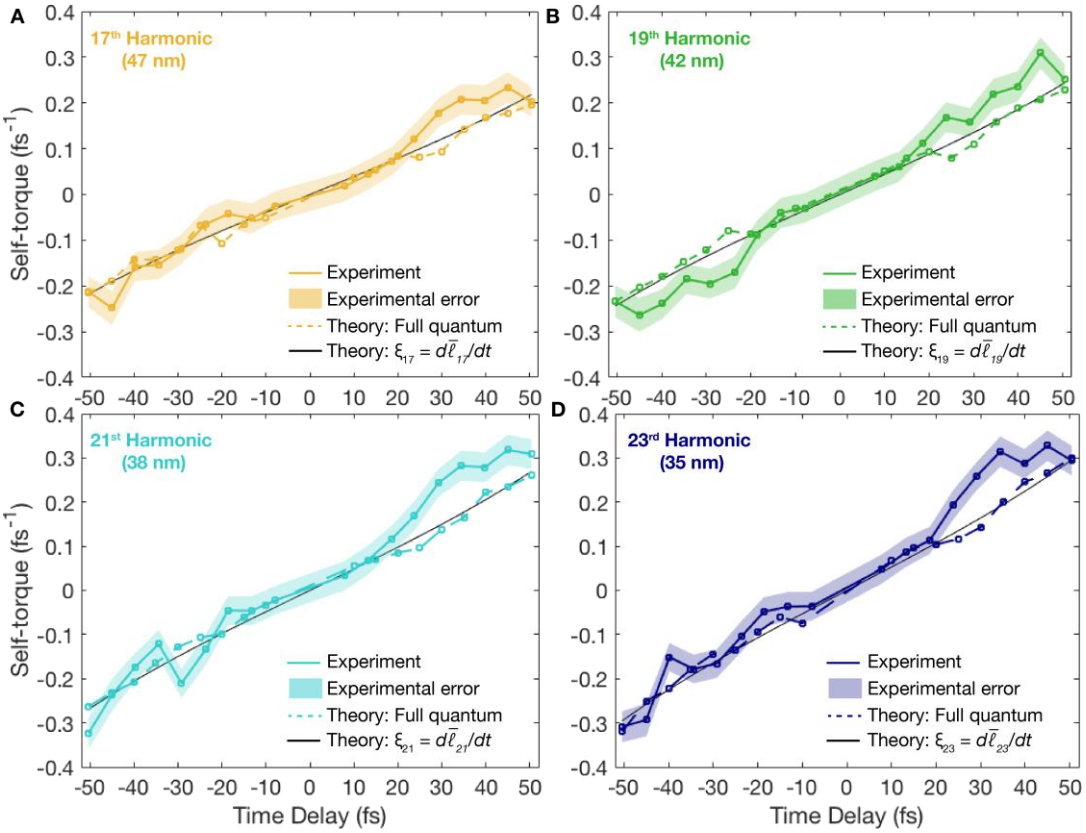

Fig. 5. Experimental Confirmation of the Self-Torque of Light in EUV Beams. Self-torques obtained as a function of the time delay between the IR laser drivers for the 17th (**A**), 19th (**B**), 21st (**C**) and 23rd (**D**) harmonics. The experimental data is shown in solid-color lines, the results from full quantum simulations in dashed lines, and the analytical estimation given by Eq. 2 in solid black lines. The shaded regions depict the experimental uncertainty in the retrieved self-torque for each harmonic order, which themselves comprise the standard "one sigma" deviation of the measured self-torque (i.e., 68% of the measured self-torque values will fall within this uncertainty range).

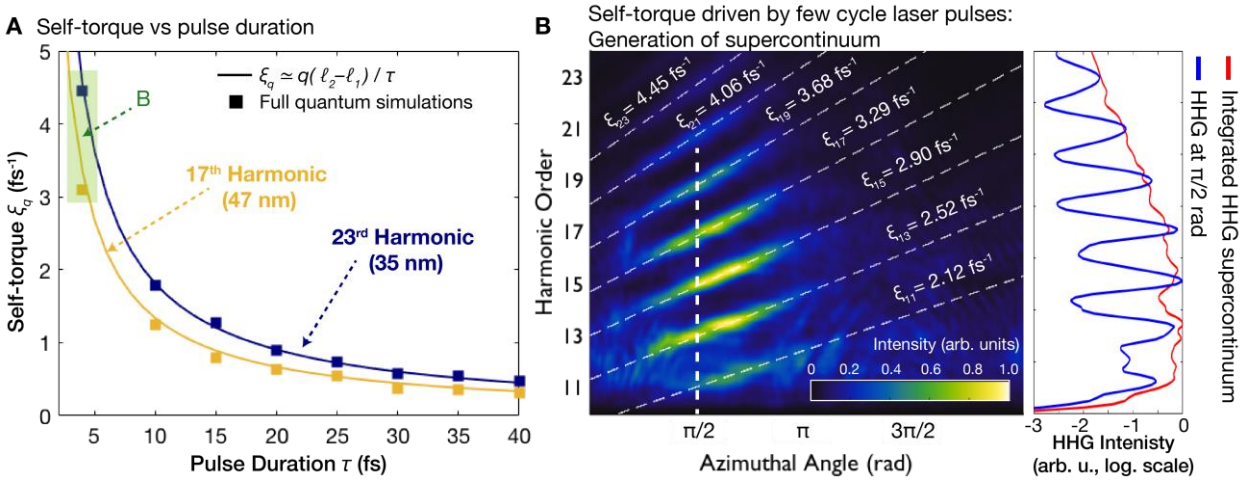

Fig. 6. Manifestation of Self-Torque for EUV Supercontinuum Generation. (**A**) Self-torque as a function of pulse duration for the 17th and 23rd harmonics, for time delays equal to their pulse duration. Solid lines are calculated from Eq. 2, and the squares correspond to results from full quantum simulations. (**B**) Spatiospectral HHG distributions when driven by two 800 nm, 4 fs pulses with ℓ_1=1 and ℓ_2=2, delayed by 4 fs with respect to each other. The optical self-torque imprints an azimuthal frequency chirp, which is different for each harmonic order, as indicated by the grey dashed lines (obtained from Eq. 5 and 6). The right panel shows the HHG yield at π/2 rad (blue line, and white vertical dashed line in **B**) and the spatially integrated supercontinuum (red line).

Main Text movie caption:

Movie 1. Comparison Between the Temporal Evolution of Phase, Intensity and OAM Content of Self-Torqued Beams and Two Delayed Vortex Beams

Temporal evolution of the phase (left column) intensity (central column) and OAM distribution along the divergence (right column) of a self-torqued beam (top) and a combination of two time-delayed vortex beams. The self-torqued beam (top) corresponds to the 11th harmonic generated through HHG ($\ell_1 = 1, \ell_2 = 2, \tau = 10$ fs, $t_d = 10$ fs, $\lambda_1 = \lambda_2 = 800$ nm) calculated using the Thin Slab Model (see Section S2 in (*54*)), whereas the vortex combination (bottom) corresponds to two time-delayed vortex beams ($\ell_1 = 11, \ell_2 = 22, \tau = 10$ fs, $t_d = 10$ fs, $\lambda_1 = \lambda_2 =$ 800 nm).